Journal of Applied Mechanics Vol.11, pp.769-778 (August 2008) JSCE

Numerical Prediction of Shielding Effects on Fluid-Forces Acting on Complicated-Shaped Object

複雑形状物体に作用する流体力の遮蔽効果に関する数値解析

Satoru USHIJIMA* and Nozomu KURODA**
牛島 省 ・ 黒田 望

*Member, Assoc. Prof. Dept. CERE, Kyoto Univ. (C-cluster, Kyoto 615-8540)
**Member, Master Course Dept. CERE, Kyoto Univ. (C-cluster, Kyoto 615-8540)

A computational method for multiphase fields, MICS [1], was applied to estimate the shielding effects on the fluid forces acting on a complicated-shaped object surrounded by other objects. In the MICS, arbitrarily-shaped objects are treated with tetrahedron elements, through which the momentum interactions between objects and fluids are accurately taken into account with a tetrahedron sub-cell method. The applicability of the MICS was discussed with the experimental results obtained in some arrangements of the objects which surround a target object in a flume equipped with a wave generator. As a result, it was shown that the MICS enables us to predict reasonably the shielding effects on the fluid forces in all cases of the present experiments.

Key Words : *fluid force, shielding effect, free-surface flow, MICS*

1. Introduction

It is important to estimate accurately the fluid forces caused by free surface flows against a complicated shaped object like a wave breaking block. In such evaluations, it is necessary to take account of the shielding effect, which means the variation of fluid forces due to the deformation of the free-surface flows caused by the surrounding objects, since it is rare that such an object exists alone in the actual conditions. Although in many cases some empirical coefficients, such as the drag and lift coefficients C_d and C_L, have been utilized in the evaluation of fluid forces, it is obvious that such evaluations are inaccurate since the empirical coefficients are usually derived in a uniform flow with a single object and the shielding effects are not taken into account.

In the present paper, a computational method for multiphase fields, MICS [1], is applied to estimate the shielding effects on the fluid forces acting on a complicated-shaped object, which is surrounded by other objects. In contrast to the usual numerical methods, the MICS enables us to deal with the free-surface flows around arbitrarily-shaped objects. Since the fluid-solid interactions are taken into account in this method, it is possible to estimate the fluid forces acting on the complicated-shaped objects as well as the shielding effects on it.

The predicted free-surface profiles and fluid forces with the MICS are compared with the experimental results, which were obtained in a flume equipped with a wave generator. Some arrangements of the objects surrounding the target object are examined and it is shown that the MICS allows us to estimate reasonably the fluid forces and shielding effects on them in all cases of the present experiments.

2. Numerical Procedures

2.1 Basic Equations

The multiphase field consisting of gas, liquid and solid phases is treated as a mixture of fluids Ω, which is the collection of the immiscible and incompressible fluids Ω_i, as shown in Fig.1. The fluid components Ω_i in Fig.1 have different physical properties equivalent to the corresponding phases. This treatment enables us to deal with the complicated-shaped objects included in free surface flows easily.

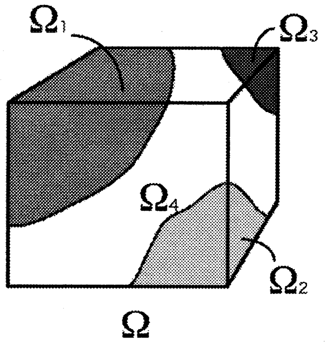

Fig. 1 Mixture of immiscible and incompressible fluids

The mass-conservation equations in the Eulerian and Lagrangian forms for the fluid mixture Ω are given as follows:

$$\sum_k \int_{\Omega_k} \left[\frac{\partial \rho_k}{\partial t} + \frac{\partial}{\partial x_j}(\rho_k u_{k,j}) \right] d\Omega = 0 \quad (1)$$

$$\sum_k \int_{\Omega_k} \left(\frac{\partial \rho_k}{\partial t} + u_{k,j} \frac{\partial \rho_k}{\partial x_j} \right) d\Omega = 0 \quad (2)$$

where ρ_k and $u_{k,i}$ are density and velocity component in the x_i direction of the fluid-k respectively. From the above two equations, the incompressible condition is derived as

$$\sum_k \int_{\Omega_k} \frac{\partial u_{k,i}}{\partial x_i} d\Omega = 0 \quad (3)$$

The momentum equation for Ω is given by

$$\sum_k \int_{\Omega_k} \left[\frac{\partial}{\partial t}(\rho_k u_{k,i}) + \frac{\partial}{\partial x_j}(\rho_k u_{k,i} u_{k,j}) \right] d\Omega$$
$$= \sum_k \int_{\Omega_k} \left[\frac{\partial \tau_{k,ij}}{\partial x_j} + \rho_k f_i \right] d\Omega + \int_{\partial I} F_{s,i}\, dS \quad (4)$$

where f_i is the acceleration component of the external force and the second term on the right-hand side of Eq.(4) means the surface integration of the surface tension $F_{s,i}$ acting in the x_i direction. The stress $\tau_{k,ij}$ is defined as

$$\tau_{k,ij} = -p_k \delta_{ij} + \mu_k e_{k,ij} \quad (5)$$

where δ_{ij}, p_k, μ_k, $e_{k,ij}$ are the Kronecker delta, pressure, viscous coefficient and deformation tensor of fluid-k, respectively.

Assuming that the volume of Ω is sufficiently small, a variable $\phi_k'(t, \boldsymbol{x})$ in each fluid is approximated as its spatially-representative value $\phi_k(t)$ as follows:

$$\int_{\Omega_k} \phi_k'(t, \boldsymbol{x})\, d\Omega \approx \int_{\Omega_k} \phi_k(t)\, d\Omega = \Omega_k \phi_k(t) \quad (6)$$

With this relationship, Eq.(1) is rewritten as

$$\frac{\partial \rho}{\partial t} + \frac{\partial}{\partial x_j}(\rho u_j) = 0 \quad (7)$$

where ρ and u_i are volume-average density and mass-average velocity component:

$$\rho = \frac{\sum_k \Omega_k \rho_k}{\Omega}, \qquad u_i = \frac{\sum_k \Omega_k \rho_k u_{k,i}}{\Omega \rho} \quad (8)$$

Similarly, with the relationship $u_{k,i} = u_i + \tilde{u}_{k,i}$, Eq.(2) is represented as

$$\frac{\partial \rho}{\partial t} + u_j \frac{\partial \rho}{\partial x_j} + \frac{1}{\Omega} \sum_k \Omega_k \tilde{u}_{k,j} \frac{\partial \rho_k}{\partial x_j} = 0 \quad (9)$$

Assuming that the third term on the left-hand side of the above equation is negligible, the following incompressible condition is derived from Eqs.(7) and (9):

$$\frac{\partial u_j}{\partial x_j} = 0 \quad (10)$$

With the similar procedures, Eq.(4) is rewritten as

$$\frac{\partial}{\partial t}(\rho u_i) + \frac{\partial}{\partial x_j}(\rho u_i u_j) = \rho f_i + \rho f_{s,i}$$
$$+ \frac{\partial \tau_{ij}}{\partial x_j} - \frac{1}{\Omega} \frac{\partial}{\partial x_j} \sum_k \Omega_k \rho_k \tilde{u}_{k,i} \tilde{u}_{k,j} \quad (11)$$

In Eq.(11), as proposed by a CSF model [2)], the surface force is treated as

$$\int_{\partial I} F_{s,i}\, dS = \rho f_{s,i} \Omega \quad (12)$$

This relationship means that the surface force is transformed to the body force. Putting the third term on the right-hand-side of Eq.(11) D_i, it is written with Eq.(5) as

$$D_i = -\frac{\partial p}{\partial x_i} + \frac{\partial}{\partial x_j} \left[\frac{\partial}{\partial x_j}(\mu u_i) + \frac{\partial}{\partial x_i}(\mu u_j) \right] \quad (13)$$

where p and μ are volume-average pressure and viscous coefficient defined as follows:

$$p = \frac{\sum_k \Omega_k p_k}{\Omega}, \qquad \mu = \frac{\sum_k \Omega_k \mu_k}{\Omega} \quad (14)$$

Finally, assuming that the non-linear term of $\tilde{u}_{k,i}\tilde{u}_{k,j}$ in Eq.(11) and surface tension are negligible, the conservative form of the momentum equation is derived as

$$\frac{\partial u_i}{\partial t} + \frac{\partial}{\partial x_j}(u_i u_j) = f_i$$
$$- \frac{1}{\rho} \frac{\partial p}{\partial x_i} + \frac{1}{\rho} \frac{\partial}{\partial x_j} \left[\frac{\partial}{\partial x_j}(\mu u_i) + \frac{\partial}{\partial x_i}(\mu u_j) \right] \quad (15)$$

The governing equations of the MICS consist of Eqs. (7), (10) and (15).

2.2 Computational Method

The discretized governing equations of the fluid-mixture are solved after determining the volume-average physical properties with the sub-cell method, which will be described later. The three-dimensional velocity components u_i and the pressure variable p of the discretized equations are defined on the collocated grid points in the computational fluid cell.

The numerical procedures of the incompressible fluid-mixture consist of three stages; prediction, pressure-computation and correction stages. At the prediction stage, the tentative velocity components u_i^* are calculated at the center of the cells with a finite-volume method. In this procedure, Eq. (15) is discretized with the C-ISMAC method [3], which is based on the implicit SMAC method [4] that allows us to decrease computational time without decreasing numerical accuracy. The equation discretized with respect to time by the C-ISMAC method is given by

$$
\begin{aligned}
\frac{u_i^* - u_i^n}{\Delta t} &= f_i - \frac{1}{\rho}\frac{\partial p^n}{\partial x_i} \\
&- \alpha\frac{\partial}{\partial x_j}(u_i^* u_j^n) - (1-\alpha)\frac{\partial}{\partial x_j}(u_i^n u_j^n) \\
&+ \frac{\beta}{\rho}\frac{\partial}{\partial x_j}\left[\frac{\partial}{\partial x_j}(\mu u_i^*) + \frac{\partial}{\partial x_i}(\mu u_j^*)\right] \\
&+ \frac{1-\beta}{\rho}\frac{\partial}{\partial x_j}\left[\frac{\partial}{\partial x_j}(\mu u_i^n) + \frac{\partial}{\partial x_i}(\mu u_j^n)\right] \qquad (16)
\end{aligned}
$$

where α and β are the parameters whose ranges are $0 \leq \alpha, \beta \leq 1$. With the following relationship,

$$u_i^* = u_i^n + \tilde{u}_i \qquad (17)$$

Eq.(16) is transformed to the following equation:

$$
\begin{aligned}
&\frac{\tilde{u}_i}{\Delta t} + \alpha\frac{\partial}{\partial x_j}(\tilde{u}_i u_j^n) - \frac{\beta}{\rho}\frac{\partial}{\partial x_j}\left[\frac{\partial}{\partial x_j}(\mu\tilde{u}_i) + \frac{\partial}{\partial x_i}(\mu\tilde{u}_j)\right] \\
&= f_i - \frac{1}{\rho}\frac{\partial p^n}{\partial x_i} - \frac{\partial}{\partial x_j}(u_i^n u_j^n) \\
&+ \frac{1}{\rho}\frac{\partial}{\partial x_j}\left[\frac{\partial}{\partial x_j}(\mu u_i^n) + \frac{\partial}{\partial x_i}(\mu u_j^n)\right] \qquad (18)
\end{aligned}
$$

where $\tilde{u}_i$ becomes nearly zero when the flow field is almost steady or the time-scale of the flow field is sufficiently larger than the time increment Δt. Thus, we can apply a simple first-order spatial discretization method to the left-hand side of Eq.(18), while higher-order scheme to the right-hand side. The convection terms are evaluated with a fifth-order conservation FVM-QSI scheme [5] and numerical oscillations are removed by a flux-control method [5]. The C-ISMAC method enables us to derive the simultaneous equation system easily from the implicit form of the left-hand side of Eq.(18) as well as to preserve numerical accuracy by applying a higher-order scheme to the explicit form on the right-hand side Eq.(18).

After solving the equation system of $\tilde{u}_i$, which is derived from the discretized equation of Eq.(18), we obtain u_i^* with Eq.(17). The u_i^* derived at the center of the computational cell is then spatially interpolated on the cell boundary. Before this interpolation, pressure-gradient term evaluated at the cell center is removed from u_i^* in order to prevent pressure oscillation as

$$\hat{u}_i = u_i^* + \frac{1}{\rho}\frac{\partial p^n}{\partial x_i}\Delta t \qquad (19)$$

The cell-center velocity $\hat{u}_i$, which does not include the pressure-gradient term, is spatially interpolated on the cell boundaries by f_b, which is a linear function in the present study. After this procedure, the pressure-gradient terms that are estimated on the cell boundaries are added to the interpolated velocity, $f_b(\hat{u}_i)$. Thus, we obtain the cell-boundary velocity component $u_{b,i}$ as follows:

$$u_{b,i} = f_b(\hat{u}_i) - \left.\frac{1}{\rho}\frac{\partial p^n}{\partial x_i}\right|_b \Delta t \qquad (20)$$

The velocity component $u_{b,i}^{n+1}$ at $n+1$ time-step is defined by

$$u_{b,i}^{n+1} = f_b(\hat{u}_i) - \left.\frac{1}{\rho}\frac{\partial p^{n+1}}{\partial x_i}\right|_b \Delta t \qquad (21)$$

Subtracting Eq.(20) from Eq.(21), we have

$$u_{b,i}^{n+1} = u_{b,i} - \frac{1}{\rho}\frac{\partial \phi}{\partial x_i}\Delta t \qquad (22)$$

where $\phi = p^{n+1} - p^n$. Substitution of Eq.(22) into the incompressible condition given by Eq.(10) that is estimated at $n+1$ time-step yields the following equation of ϕ :

$$\frac{\partial}{\partial x_i}\left(\frac{1}{\rho}\frac{\partial \phi^k}{\partial x_i}\right) = \frac{1}{\Delta t}\frac{\partial u_{b,i}}{\partial x_i} \equiv \frac{D}{\Delta t} \qquad (23)$$

At the pressure-computation stage, Eq.(23) is solved with the C-HSMAC method. The C-HSMAC method enables us to obtain the pressure and cell-boundary velocity components, which satisfy the incompressible condition $|D| < \epsilon_D$ in each computational cell, where ϵ_D is a given threshold. While the final results of the C-HSMAC method are similar to those of the SOLA or HSMAC method [6], it has been proved that the computational efficiency of the C-HSMAC method is largely improved [1]. The relationships in the C-HSMAC method are given by

$$\frac{\partial}{\partial x_i}\left(\frac{1}{\rho}\frac{\partial \phi}{\partial x_i}\right) = \frac{D^k}{\Delta t} \tag{24}$$

$$p^{k+1} = p^k + \phi \tag{25}$$

$$u_{b,i}^{k+1} = u_{b,i}^k - \frac{\Delta t}{\rho}\frac{\partial \phi}{\partial x_i} \tag{26}$$

where the superscript k stands for the iteration step-number of the C-HSMAC method. The initial values of $u_{b,i}^k$ and p^k are $u_{b,i}$ given by Eq.(20) and p^n respectively.

The discretization of Eq.(24) yields simultaneous linear equation system of ϕ, which is solved with the BiCGSTAB method [7]. The iterative computation using the above three equations is completed when $|D| < \epsilon_D$ is satisfied in all cells.

2.3 Sub-Cell Method

As shown in the derivation of the governing equations, the physical values of the mixture of fluids need to be determined for each computational cell. Since the computational cell is based on the Eulerian grid which is fixed in the space, the volume-average physical value ψ in the cell is estimated with the following equation:

$$\psi = (1-f)\psi_g + \left(f - \sum_{P_k \in C} \alpha_k\right)\psi_l + \sum_{P_k \in C} \alpha_k \psi_{bk} \tag{27}$$

where ψ_g and ψ_l are physical values in the gas and liquid phases respectively and ψ_{bk} is that of the object$-k$. The volume fraction of the liquid and solid phases in a computational fluid cell is given by f and the fraction of the solid part is defined by α_k. The fraction α_k is approximated with a sub-cell method, as shown in Fig.2. As shown later, a solid object is represented by multiple tetrahedron elements. When the element is completely included in a single fluid cell as shown in Fig.2 (a), α_k is easily determined from the element volume. In contrast, when the element is included in multiple fluid cells as shown in Fig.2 (b), a fluid cell is divided into multiple sub-cells and α_k is determined from the number of sub-cells included in the element, which are shown as gray cells in Fig.2 (b). The accuracy of the sub-cell method can be improved using the smaller sub-cells.

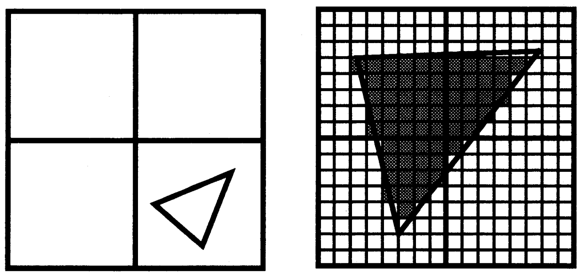

(a) Tetrahedron element included in a fluid cell (b) Tetrahedron element in multiple fluid cells

Fig. 2 Sub-cell method (thick grid lines stand for fluid cell and thin lines in (b) indicate sub-cells)

2.4 T-Type Solid Model

A solid object in the flow is numerically represented using T-type solid model. The object surface model, created with a CAD software as shown in Fig.3 (a), is divided into multiple tetrahedron elements shown in Fig.3 (b). Compared with the "sphere-connected model", which represents an object with multiple sphere elements, T-type model is advantageous in respect that its approximations of volume, mass and inertia tensors are more accurate. The contact spheres, shown in Fig.3 (c), are used only in the collision detection between objects.

2.5 Movements of Solid Objects

The movements of the T-type solid model are calculated with the basic equations for translational and rotational motions. The basic equation of the translational motion is given by

$$M_b \dot{\boldsymbol{v}} = \boldsymbol{F} \tag{28}$$

where M_b is the mass of an object, $\boldsymbol{v}$ is the velocity vector of its center and dot means time differentiation.

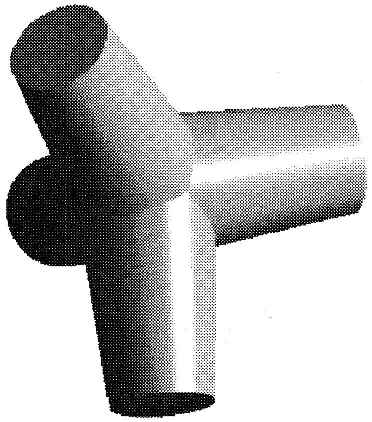

(a) Surface model

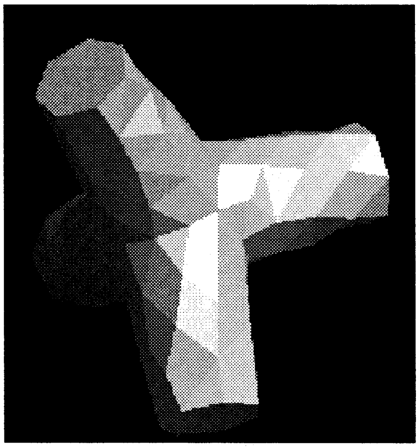

(b) Polygon model

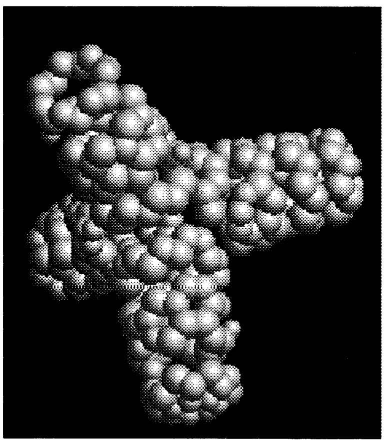

(c) Contact spheres

Fig. 3 T-type solid model

The basic equation of the rotational motion, Euler equation, can be written as the following form:

$$\dot{\boldsymbol{\omega}} = \boldsymbol{I}^{-1}\left[R^{-1}\boldsymbol{N} - \boldsymbol{\omega} \times \boldsymbol{I}\boldsymbol{\omega}\right] \tag{29}$$

where $\boldsymbol{\omega}$ is the angular velocity vector, $\boldsymbol{I}$ is inertia tensor in the basic attitude of the object, R is a rotation matrix and $\boldsymbol{N}$ is the external torque imposed on the object. The numerical processes related to the rotation are actually performed with quaternions instead of the multiplication of the matrix R. The location and attitude of the object are determined form Eqs.(28) and (29).

2.6 Fluid Forces Acting on Objects

The fluid forces acting on the objects are calculated with the pressure and viscous terms obtained from the computational results of Eq. (15):

$$F_{Cki} = \alpha_k \sigma_k \Delta C \cdot \left[-\frac{1}{\rho}\frac{\partial p}{\partial x_i} + \frac{1}{\rho}\frac{\partial}{\partial x_j}\left\{\frac{\partial}{\partial x_j}(\mu u_i) + \frac{\partial}{\partial x_i}(\mu u_j)\right\}\right] \tag{30}$$

where $\boldsymbol{F}_{Ck}$ is the fluid force vector in fluid cell C acting on object$-k$ and its x_i component is given by F_{Cki}. The component F_{Cki} is calculated from Eq. (30) with the volume of a fluid cell ΔC, density of the body σ_k and volume fraction α_k calculated with the sub-cell method.

In the T-type solid model, as shown in Fig.4, the summation of $\boldsymbol{F}_{Ck}$ in all fluid cells is the force vector $\boldsymbol{F}$ on the right hand side of Eq. (28). Similarly, the torque $\boldsymbol{N}$ in Eq. (29) is obtained from the summation of the moments $\boldsymbol{r}_{GC} \times \boldsymbol{F}_{Ck}$, where $\boldsymbol{r}_{GC}$ is the vector from the object center $\boldsymbol{x}_{c,k}$ to the center of a fluid cell C as shown in Fig.4.

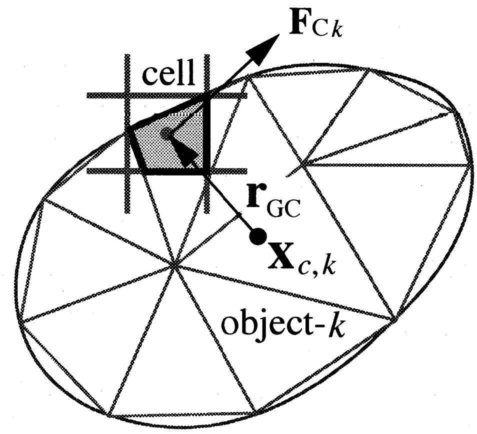

Fig. 4 Fluid force acting on a tetrahedron element in a fluid cell

3. Application of prediction method

3.1 Experiments

The fluid forces acting on the target object surrounded by multiple objects were measured in a wave-generator flume, in order to understand the shielding effects on the fluid forces.

The schematic view of the flume equipped with a wave generator is shown in Fig.5. The horizontal movements of the vertical plate on the left side of the flume can be controlled by a PC, so that it can generate the wave flows above the box fixed on right side of the flume. The target object and the surrounding objects are placed on the box as detailed later.

The lengths L_1 and L_2 of the flume are both 0.7 m. The width of the flume B is 0.19 m. The height of the box in the flume h_b is 0.1 m and the width of the flume is 0.19 m. The initial water depth h_0 was set at 0.104 m and the water level is same as the height of the bottom edge of the target object. The maximum water depth due to the generated wave was about 147 mm at the point 100 mm apart from the front edge of the box.

The target object, as shown in Fig.6, is a four-leg wave breaking block, whose height is about 56 mm and specific density is around 2.14. The target object was supported by a steel plate on which four strain gages are fixed to measure the streamwise component of the fluid forces acting on the object. On the other hand, the other objects surrounding the target block are six-leg blocks as shown in Fig.7. The side length d shown in Fig.7 is about 20 mm.

Three cases of experiments were carried out with the different arrangements of the surrounding blocks, as shown in Fig.8. In case-F, three six-leg blocks are placed in front of the target four-leg block. Similarly, three six-leg blocks are fixed behind the target block in case-B. In case-S, two six-leg blocks are placed next to the target block as shown in Fig.8. The positions of the surrounding blocks are shown in Fig.9. The distances of the block edges from the side walls, b_1 and b_2 are 10 mm and 15 mm respectively, while the distance from the front end of the box, d_1 and d_2 are 100 mm and 50 mm respectively. The attitudes of the surrounding blocks in case-S are different from case-F and case-B, so that they can approach the target block as much as possible in case-S.

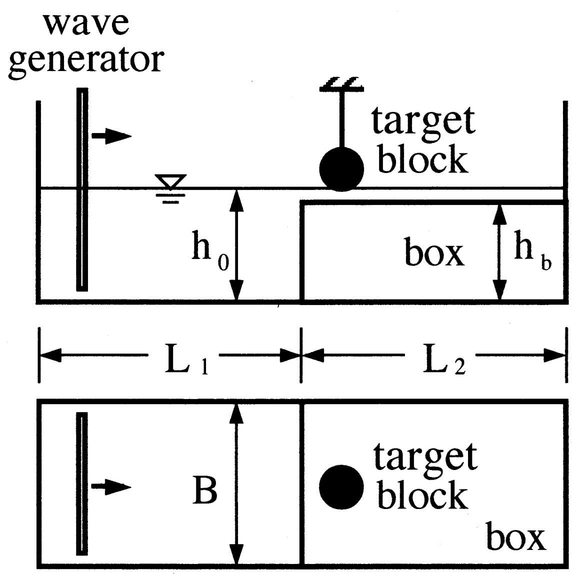

Fig. 5 Experimental flume (plane and side views)

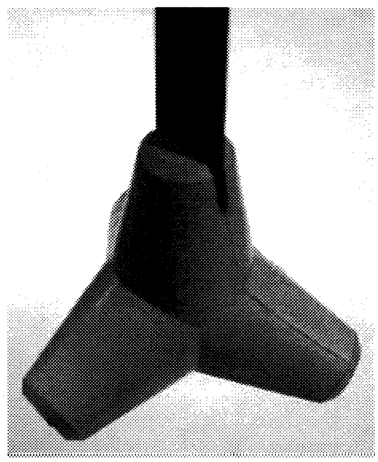

Fig. 6 Target four-leg block with supporting plate

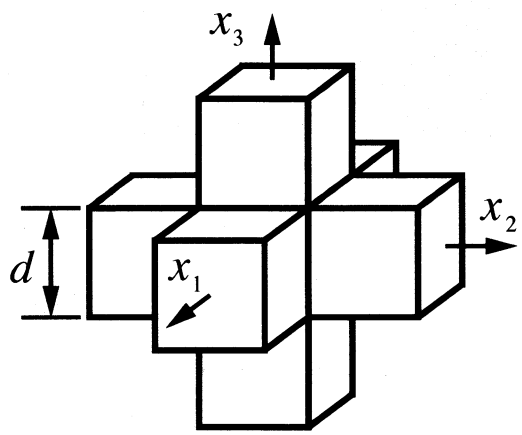

Fig. 7 Six-leg block

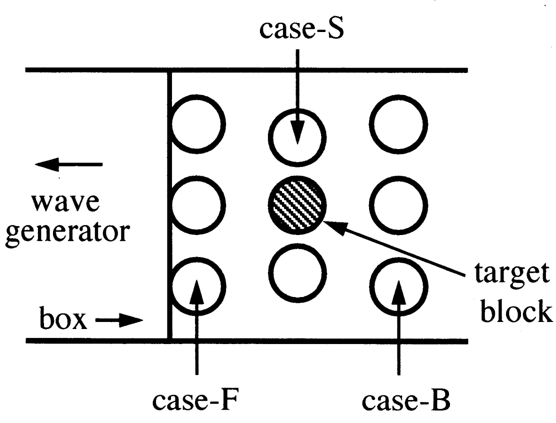

Fig. 8 Arrangement of surrounding blocks

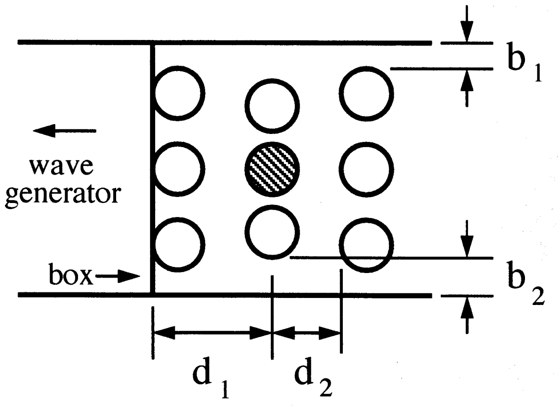

Fig. 9 Positions of the surrounding blocks

3.2 Conditions of computations

In the numerical predictions, $140 \times 38 \times 50$ computational cells are set up in the three-dimensional volume of $1.4 \times 0.19 \times 0.25$ m, including the air region. The initial conditions are same as those of the experiments. The unsteady computations proceed with time increment $\Delta t = 1.0 \times 10^{-2}$ second.

The numerical models for the blocks were created with the CAD software and a mesh generator to set up the tetrahedron elements. The target block is represented with 416 tetrahedron elements and 152 node points, while the surrounding six-leg block consists of 244 elements and 78 nodes. The tetrahedron sub-cell number was 125 in each fluid cell. The kinematic viscosity of the water and air were set at 1.0×10^{-6} and 1.0×10^{-5} m^2 / sec., respectively. The density of the blocks in the computations are same as that of the experiments.

3.3 Comparison between experiments and predictions

The computational results obtained with only a single target block are shown in Fig.10 and Fig.11, which are taken from our previous paper [8]. It has been confirmed that the agreements of the time histories for the fluid forces shown in Fig.11, acting in the streamwise direction, are satisfactory in case that there is no surrounding objects.

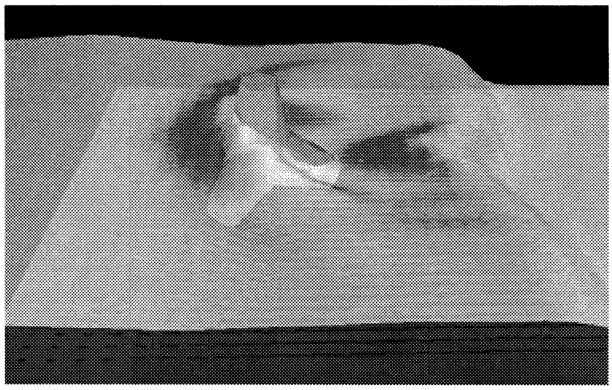

Fig. 10 Predicted free-surface profiles around a single block, t = 1.1 (s)

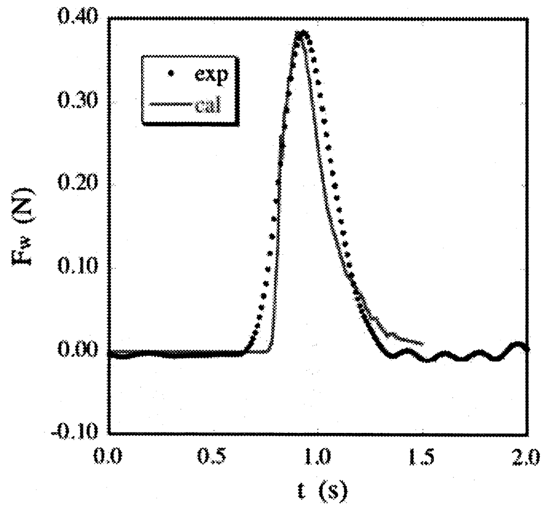

Fig. 11 Time histories of fluid forces acting on a single block

On the other hand, the predicted free surface profiles obtained in case-F, case-S and case-B are shown in Fig.12, Fig.13 and Fig.14, respectively. It can be seen that the wave flows are largely distorted due to the existence of the surrounding blocks.

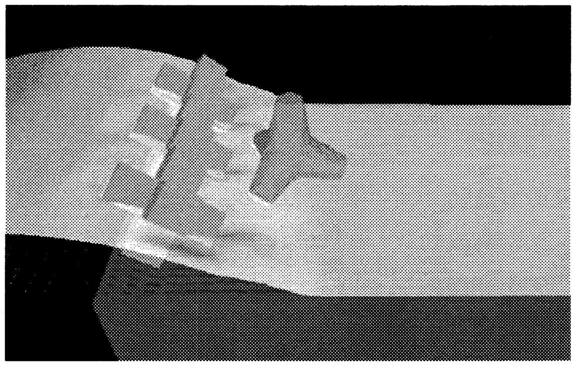

(a) $t = 0.9$ (s)

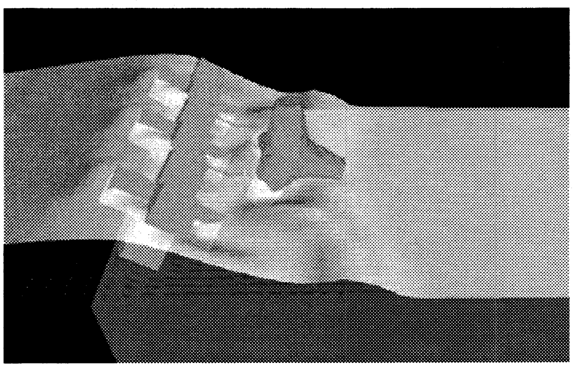

(b) $t = 1.0$ (s)

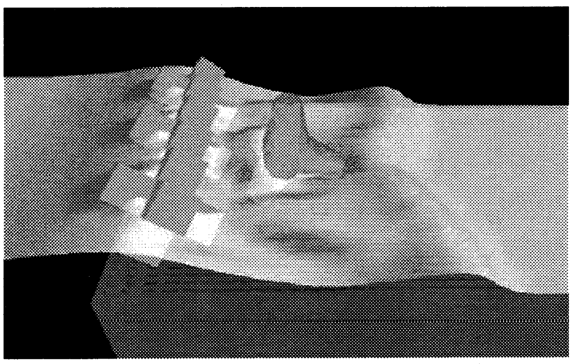

(c) $t = 1.1$ (s)

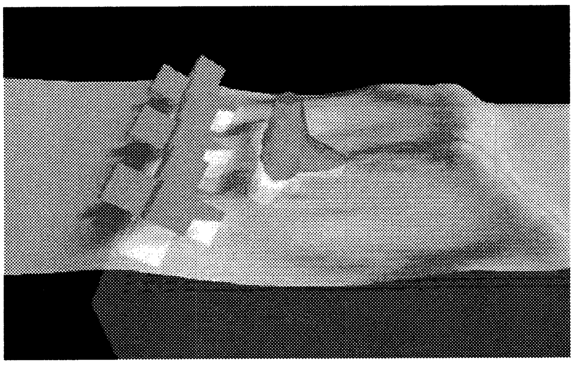

(d) $t = 1.2$ (s)

Fig. 12 Predicted results of free-surface flows (case-F)

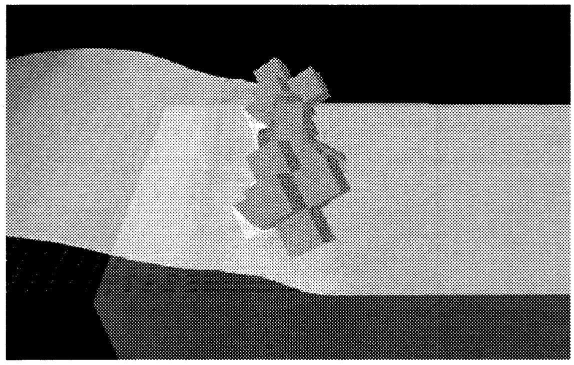

(a) $t = 0.9$ (s)

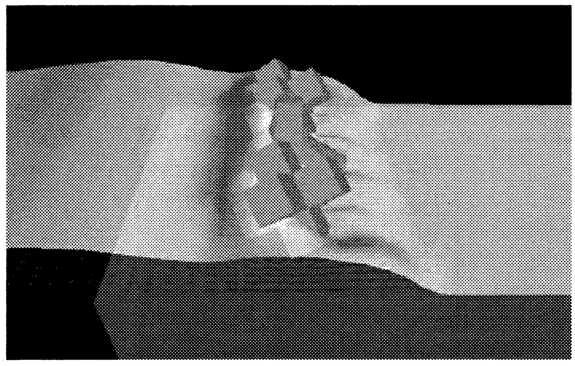

(b) $t = 1.0$ (s)

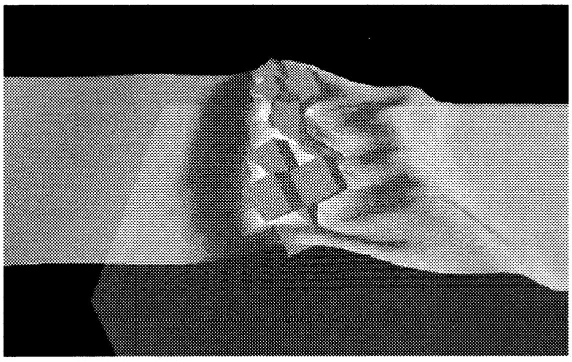

(c) $t = 1.1$ (s)

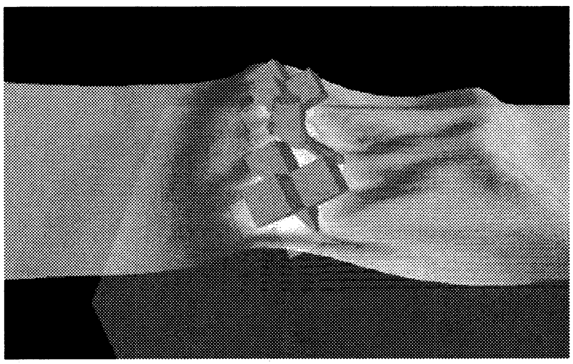

(d) $t = 1.2$ (s)

Fig. 13 Predicted results of free-surface flows (case-S)

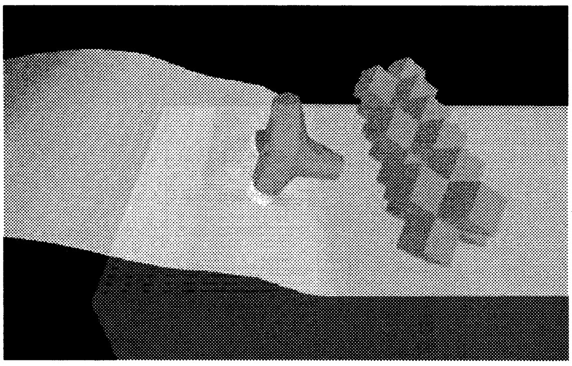

(a) t = 0.90 (s)

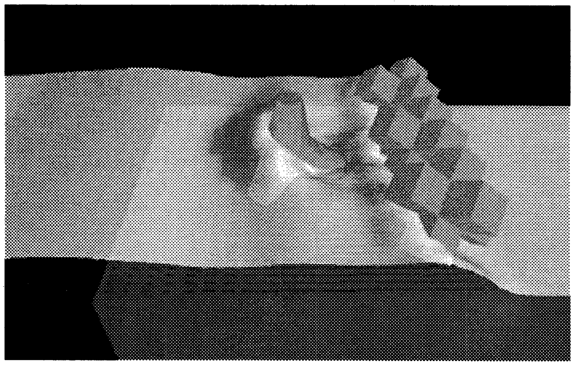

(b) t = 1.05 (s)

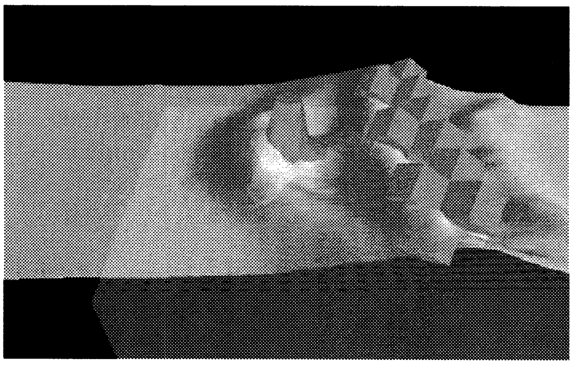

(c) t = 1.20 (s)

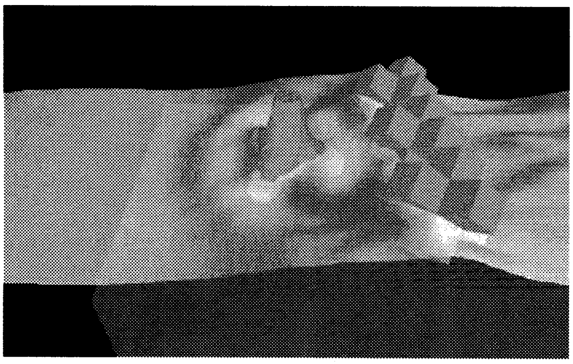

(d) t = 1.35 (s)

Fig. 14 Predicted results of free-surface flows (case-B)

In case-F, as shown in Fig.12, the wave flows are trapped by the three six-leg blocks in front of the target block. Thus the free surface level in front of the target block in Fig.12 (c), which was taken at t = 1.1 sec., is smaller than that of the single target block shown in Fig.10. It can be seen that the shielding effects of three six-leg blocks are so large that only the weakened wave flows that pass through them collide with the target block.

The time histories of the fluid forces against the target block in case-F are shown in Fig.15. It is obvious that the peak value of the fluid forces is about 1/3 compared with the maximum value shown in Fig.10. It is also seen that the experimental values and predictions shown in Fig.15 are in good agreement. Conclusively, the shielding effects in case-F are reproduced well in the present computational method.

On the other hand, in case-S shown in Fig.13, since there are no obstacles in front of the target block, the wave flows acting on it are almost same as those in the case of the single block as shown in Fig.10. However, the flows passing through the side of the target block are trapped by two six-leg blocks next to the target one. This fact makes the velocity and pressure distributions around the target block different from the single block as shown in Fig.10. Thus, the maximum value of the fluid forces shown in Fig.16 is slightly smaller than that in Fig.11. The shielding effect is certainly admitted in case-S, while the influence is smaller than case-F.

Similarly to case-S, there are no obstacles in front of the target block in case-B, as shown in Fig.14. Nevertheless, it can be thought that the flow conditions are different from the single block in the following two points: 1) the gradient of water level and the fluid velocity become smaller due to the six-leg blocks behind the target one, and 2) the reflected waves occur due to the blocks behind. As shown in Fig.17, the peak value of the fluid forces is smaller than that in Fig.11 due to the above effect 1). In addition, it is demonstrated that the negative fluid force occurs in the experimental results in Fig.17 following the positive one. The negative fluid force is caused by the reflected wave flows due to the effect 2). This negative fluid force is also predicted in Fig.17, while it is underestimated compared with the experiments.

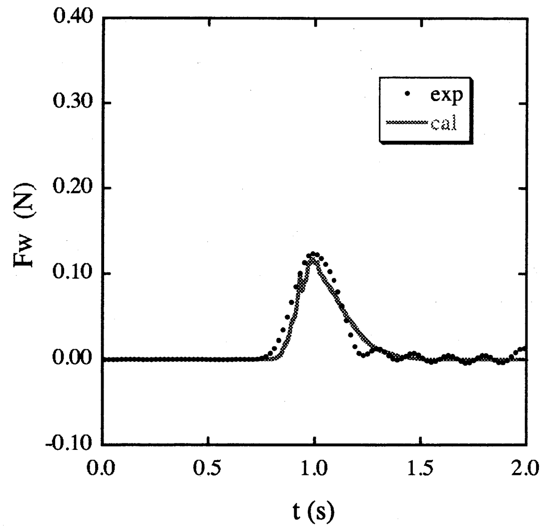

Fig. 15 Time histories of fluid forces in case-F

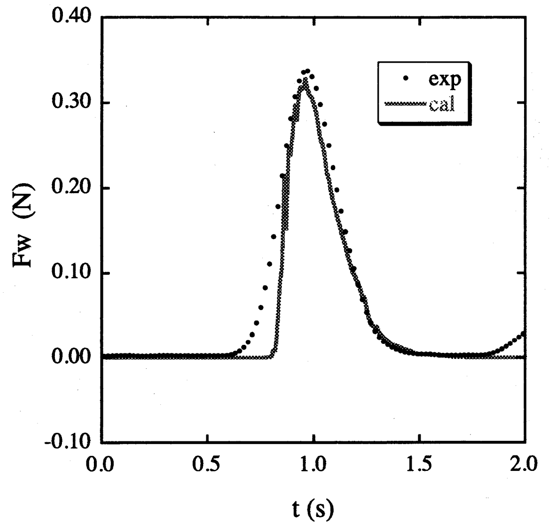

Fig. 16 Time histories of fluid forces in case-S

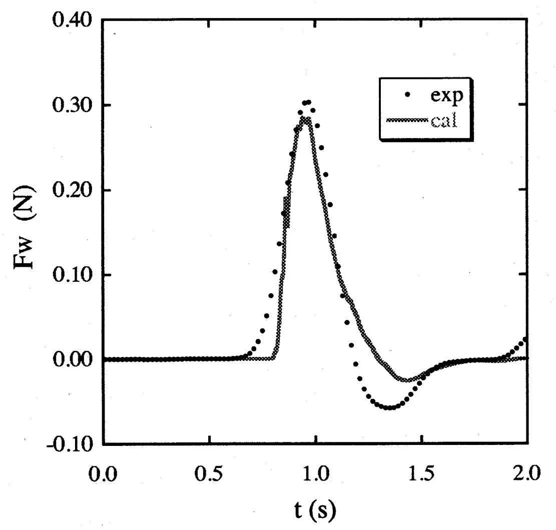

Fig. 17 Time histories of fluid forces in case-B

The shielding effect is also admitted to some extent in case-B, meanwhile the fluid forces due to the reflected waves are additionally caused by the blocks behind.

4. Conclusion

The computational method MICS was applied to estimate the shielding effects on the fluid forces acting on a complicated-shaped object surrounded by other objects. The predicted free surface profiles and fluid forces for three arrangements of the surrounding objects, case-F, S and B, were discussed with the experimental results. It has been shown that the MICS enables us to predict reasonably the shielding effects on the fluid forces in all three cases, which seems to be difficult to predict with the usual computational methods.

REFERENCES

1) S. Ushijima, S. Yamada, S. Fujioka, and I. Nezu. Prediction method (3D MICS) for transportation of solid bodies in 3D free-surface flows. *JSCE Journal*, Vol. 810/II-74, pp. 79–89, 2006.
2) J. U. Brackbill, D. B. Kothe, and C. Zemach. A continuum method for modeling surface tension. *J. Comput. Phys.*, Vol. 100, pp. 335–354, 1992.
3) S. Ushijima and I. Nezu. Higher-order implicit (C-ISMAC) method for incompressible flows with collocated grid system. *JSCE Journal*, No. 719/II-61, pp. 21–30, 2002.
4) B. R. Shin, T. Ikohagi, and H. Daiguji. An unsteady implicit SMAC scheme for two-dimensional incompressible Navier-Stokes equations. *JSME International Journal*, Vol. 36, No. 4, pp. 598–606, 1993.
5) S. Ushijima, K. Yoshida, M. Takemura, and I. Nezu. Fifth-order conservative scheme with flux control applicable to convection equations. *JSCE Journal*, No. 747/II-65, pp. 85–94, 2003.
6) C. W. Hirt and J. L. Cook. Calculating three-dimensional flows around structures and over rough terrain. *J. Comput. Phys.*, Vol. 10, pp. 324–340, 1972.
7) H. A. Van Der Vorst. BI-CGSTAB : A first and smoothly converging variant of BI-CG for the solution of nonsymmetric linear systems. *SIAM J. Sci. Stat. Comput.*, Vol. 13, pp. 631–644, 1992.
8) S. Ushijima, N. Yoshikawa, N. Yoneyama, and I. Nezu. Numerical prediction for fluid forces acting on 3D complicat ed-shaped objects in free-surface flows. *Annual Journal of Hydraulic Engineering, JSCE*, Vol. 52, pp. 955–960, 2008.

(Received April 14, 2008)